Scalability of Gadolinium-Doped-Water Cherenkov Detectors for Nuclear Nonproliferation

Viacheslav A. Li[*], Steven A. Dazeley, Marc Bergevin, and Adam Bernstein

Lawrence Livermore National Laboratory, Livermore, California 94550

Antineutrinos are an inextricable element of the fission process. The kiloton-scale KamLAND experiment has demonstrated a capability to detect reactor antineutrinos at a range of a few hundred kilometers. But to detect or rule out the existence of a single small reactor over many kilometers requires a large detector, so large in fact that the optical opacity of the detection medium itself becomes an important factor. If the detector is so large that photons cannot traverse the detector medium to an optical detector, then it becomes impractical. For this reason, gadolinium-doped-water Cherenkov detectors have been proposed for large volumes, due to their appealing light-attenuation properties. Even though Cherenkov emission does not produce many photons and the energy resolution is poor, there may be a place for Gd-doped-water detectors in far-field nuclear-reactor monitoring. In this paper, we focus on the reactor-discovery potential of large-volume Gd-doped-water Cherenkov detectors for nuclear-nonproliferation applications. Realistic background models for the worldwide reactor flux, geoneutrinos, cosmogenic fast neutrons, and detector-associated backgrounds are included. We calculate the detector run time required to detect a small 50-MWt reactor at a variety of stand-off distances as a function of detector size. We highlight that, at present, the photomultiplier-tube dark rate and event reconstruction algorithms are the limiting factors to extending such detectors beyond a fiducial mass of approximately 50 kt.

I. INTRODUCTION

Nuclear reactors produce enormous numbers of antineutrinos as a consequence of the production of beta-decaying neutron-heavy fission daughter products. In fact, a typical large nuclear-power reactor (approximately 1 GWt) generates more than approximately 10^{19} fissions per second and approximately 10^{20} antineutrinos per second during normal operation. Each fissioning isotope produces its own spectrum of daughter isotopes. Therefore, the resulting antineutrino flux and energy spectrum are sensitive to the fuel content [1]. Furthermore, since antineutrinos interact only weakly with matter, they are impossible to shield [2]. Therefore, information about the operational status and fuel content of a reactor can in principle be monitored remotely at significant distances via the antineutrino flux.

Although the growth in the worldwide number of reactors since the mid 1980s has been slow, about 500 nuclear-power reactors worldwide currently account for approximately 10% of global electricity production. Despite it being a carbon-free energy source, one of the reasons for the slow growth rate of nuclear power is the enormous capital cost of building a new nuclear reactor. Future reactor designs address this issue by attempting to go smaller and simpler. Small modular reactors are designed to be simpler to operate and to reduce capital costs [3,4]. Some new reactor designs utilize smaller fuel elements or liquid fuel. These designs may be more difficult to safeguard using present-day techniques, which emphasize item accountancy.

Recently, methods for monitoring the operational status of future reactor designs have been proposed that do not rely on item accountancy. One such method is to monitor the antineutrino emissions of these reactors. The reality is, however, that antineutrinos are extremely difficult to detect, for the same reasons as those for which they are impossible to shield [5]. The range over which it is practical to monitor a reactor will be limited by cost considerations related to detector size and the requirement to place such detectors underground to shield them from cosmic-ray-induced backgrounds.

In recent years, reactor-antineutrino detectors have been deployed at 1–2 km distances to measure neutrino-oscillation properties [6–10], and a 1-kt detector called KamLAND was situated at a flux-weighted average distance of approximately 180 km from Japan's reactor fleet to study oscillations at long range [11]. In the very near future, the JUNO detector will commence operations at a distance of 53 km from two reactor complexes in China
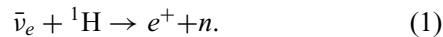
---

*li68@llnl.gov

[12], while the SNO+ detector, in Canada, will be able to observe several CANDU reactors with an effective baseline of a few hundred kilometers [13]. All of these experiments use a liquid organic scintillator as the detection medium. The fundamental limit on the size of these detectors is the attenuation of light, which is approximately 10–20 m in a liquid scintillator.

Gd-doped water is another medium for reactor-antineutrino detection, and makes use of Cherenkov light instead of scintillation light. One existing example is Super-Kamiokande [14], which has completed an initial fill of Gd-H_2O using gadolinium sulfate octahydrate at approximately one tenth of the goal concentration of 0.2% by mass. While Cherenkov emission produces less light with poorer energy resolution, attenuation lengths approaching approximately 100 m are achievable with Gd-doped water, which might enable very large detectors [15].

In 2015, the WATCHMAN collaboration proposed to demonstrate monitoring of a single reactor site using the Hartlepool reactor, with a detector to be deployed 26 km away in the Boulby mine [16]. Planning for this effort ceased following a UK government announcement in 2021 of premature shutdowns of the Hartlepool and other reactors, which would have compromised the deployment schedule for the Boulby site.

Gadolinium-doped water is sensitive to electron antineutrinos via the inverse beta-decay (IBD) reaction,

$$\bar{\nu}_e + {}^1\text{H} \rightarrow e^+ + n. \qquad (1)$$

For reactor antineutrinos, the prompt positrons (e^+) have an energy of a few MeV. The Cherenkov light from the positrons is detectable; however, the resulting 511-keV gammas do not deposit sufficient energy to generate Cherenkov light [17,18]. The neutrons are captured primarily by ^{155}Gd or ^{157}Gd, producing a few gamma rays with energies of a few MeV each [19,20], which sum to 8 MeV. The gammas are then Compton scattered, producing sufficient Cherenkov light to permit detection of a delayed event. The average delay between the positron flash and the thermal-neutron capture depends on the concentration of gadolinium in the water. At 0.1%, the neutron capture time is approximately 30 μs.

To collect the Cherenkov photons, the detector requires a sufficiently high coverage of photosensors. In Super-Kamiokande, about 40% of the detector wall area is effectively covered with photomultiplier tubes (PMTs). Light attenuation is on the order of a few hundred meters [21,22] at the blue wavelength suitable for PMT detection in large detector volumes. At energies of a few MeV, only a handful of photoelectrons (PEs) are produced. So, in addition to high photocathode coverage of the detector, a high quantum efficiency, low radioactivity, and low dark noise are desired characteristics of the PMTs.

TABLE I. Global research efforts on Gd-H_2O technology. Gadolinium is added in the form of either gadolinium chloride or gadolinium sulfate, and has natural isotopic abundances (no isotopic enrichment). For WATCHMAN and Super-Kamiokande (Super-K), a corresponding fiducial mass is also listed in square brackets.

Project	Mass (tonne)	Gd content	Ref.
Watanabe *et al.*	0.002	0.2 wt % GdCl$_3$	[25]
WAND	1.0	0.4 wt % GdCl$_3$	[26]
ANGRA	1.3	0.2 wt % GdCl$_3$	[27]
WATCHBOY	2	0.2 wt % GdCl$_3$	[28]
ANNIE	26	0.2 wt % Gd$_2$(SO$_4$)$_3$	[29]
EGADS	200	0.2 wt % Gd$_2$(SO$_4$)$_3$	[15]
WATCHMAN	6000 [1000]	0.2 wt % Gd$_2$(SO$_4$)$_3$	[16]
Super-K-Gd	50 × 10^3 [22.5 × 10^3]	0.2 wt % Gd$_2$(SO$_4$)$_3$	[14]

For nonproliferation and science alike, Gd-doped water may be a cost-efficient and environmentally friendly alternative compared with liquid-scintillator-based detectors. In the early 2000s, there were several proposals to dope water Cherenkov detectors with gadolinium in order to make them sensitive to the inverse-beta-decay reaction [23,24]. Since then, many projects have been pursued to study the feasibility of the technique, summarized in Table I. Measurements of the effect of Gd doping on water transparency have been performed with EGADS [15], the largest engineering and physics demonstration to date.

The number of IBD interactions inside a detector located at some distance from a reactor source can be calculated as follows. Each fission results in approximately 6 antineutrinos on average. Approximately a quarter of these are above the IBD 1.8-MeV threshold. Since the antineutrinos are emitted isotropically, the IBD interaction rate can be estimated as

$$N_{\text{IBD}} \cong 1.5 P_{\text{surv}} \times \left(\frac{\text{power}}{50 \text{ MWth}} \right) \times \left(\frac{\text{mass}}{10 \text{ kt}} \right)$$
$$\times \left(\frac{\text{time}}{1 \text{ day}} \right) \times \left(\frac{\text{distance}}{10 \text{ km}} \right)^{-2}, \qquad (2)$$

where P_{surv} is a probability that an electron antineutrino will retain its flavor—the so-called survival probability. It is important to note that the survival probability is a function of the antineutrino energy and distance. The survival-probability factor P_{surv}, due to neutrino oscillations, can contribute a suppression by a factor of a few, depending on the energy and stand-off distance. For example, the effect of oscillations is especially pronounced for 5-MeV antineutrinos at a distance of approximately 100 km, as shown in Fig. 1.

As shown in Ref. [32], for the purposes of nuclear nonproliferation, even a relatively small reactor of 50
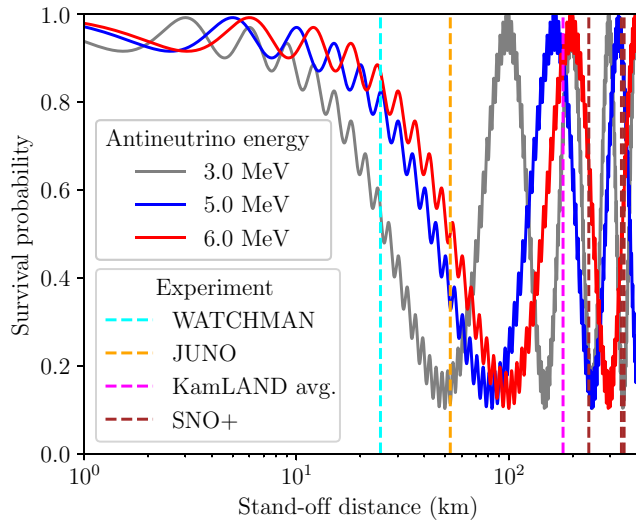
FIG. 1. Survival probability of electron antineutrinos as a function of distance, with a number of far-field-detector baselines shown (for KamLAND, a flux-weighted average baseline is plotted). Antineutrinos with energies higher than about 4 MeV become visible in a water Cherenkov detector. These are significantly suppressed at distances of approximately 50–10 km (the "death valley" for reactor antineutrinos).

MW thermal power is capable of producing a significant quantity of plutonium (8 kg) in one year. With the assumptions of 100% detection efficiency and zero detector background, that study provided estimates of the time required to detect such a reactor under various world-reactor-background conditions. By contrast, the present paper takes into account more realistic efficiency estimates and detector-related backgrounds; thus, the dwell times obtained are longer but might be considered more realistic. To account for the sometimes large variations in the world-wide reactor-antineutrino background, the same three test locations are assumed here: Andes, Baksan, and Fréjus. The closest power reactor at the Andes location is 563 km away, at Baksan it is 360 km away, and at Fréjus it is 133 km away. The world reactor background varies by approximately a factor of 100 between "low," "medium," and "high" test locations, as listed in Table II.

Figure 2 shows the antineutrino flux spectrum, the IBD interaction cross section, and the IBD interaction spectrum that can be expected from a hypothetical 50-MWt test reactor located at a distance of 20 km from a hypothetical detector. The antineutrino spectrum from our test reactor is calculated based on the reactor power, the fuel content, and the distance to the detector. Neutrino oscillations become a significant factor in the far field. Figure 3 shows the antineutrino spectrum normalized by $1/L^2$, and folded with antineutrino survival probability. Note that the antineutrino fluxes for 100- and 200-km baselines are comparable above a 5-MeV antineutrino energy, due primarily
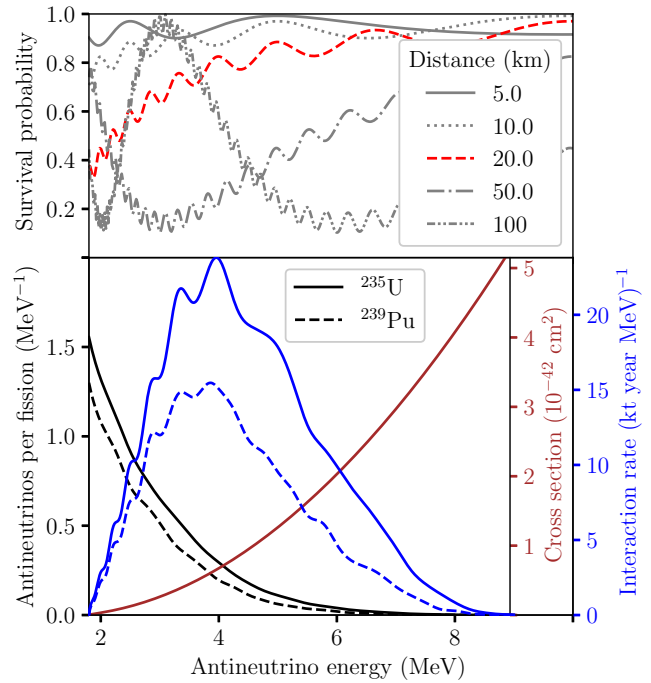

FIG. 2. The antineutrino spectrum at the detector location is expected to have the form shown by the blue lines, which takes into account the emitted spectrum, the fission energy per isotope, the antineutrino survival probability, and the IBD cross section. The full Strumia-Vissani approximation for the IBD cross section [30] and the Huber model for the emitted reactor spectrum [31] are shown. The IBD interaction rates in a kilotonne water detector from a 50-MWt reactor at a 20-km stand-off distance with two hypothetical cores are shown, with a 100% ^{239}Pu fission fraction (dashed blue line) and a 100% ^{235}U fission fraction (solid blue line); the rate for a realistic core would lie in between these two curves. The top panel shows the survival probability of reactor antineutrinos as a function of antineutrino energy for selected stand-off distances; the 20-km curve, highlighted in red, is folded to get the interaction rate shown in the bottom plot (blue curves).

to the effect of oscillations. The low-energy antineutrinos are impacted by detector-threshold effects in large water Cherenkov detectors. These detector-threshold effects are illustrated in Fig. 3, and will be further detailed in Sec. II.

TABLE II. Total world reactor background rates, in units of IBD interactions per kilotonne of water per year, for three representative locations that have high, medium, and low reactor-antineutrino fluxes. The rate for the closest reactor (CR) and its distance are also listed for each location.

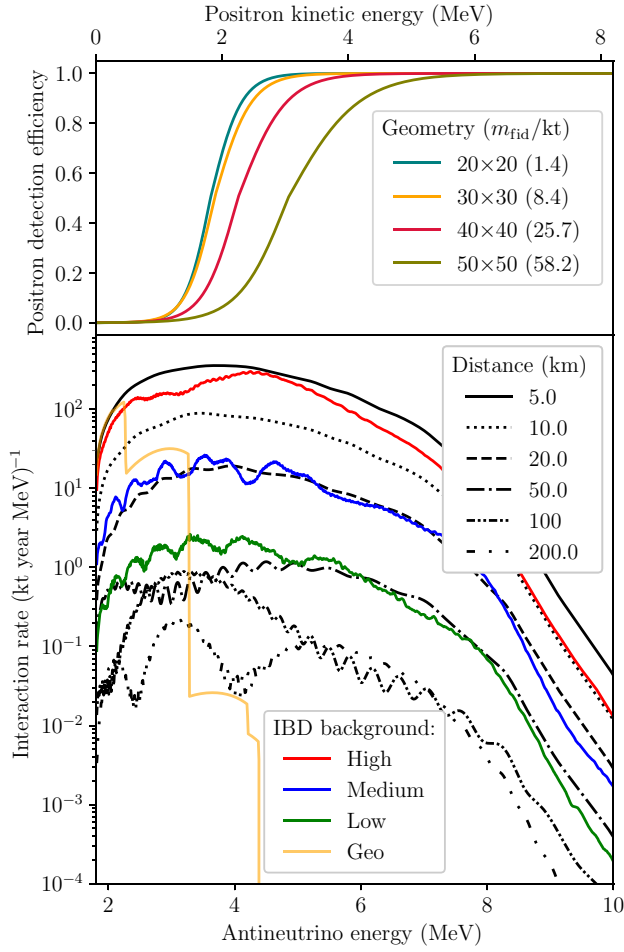| Background	Total rate	CR rate	CR distance (km)
Low	6.6	1.6	563
Medium	65.4	2.5	360
High	798.7	64.3	133

FIG. 3. IBD interaction rate as a function of antineutrino energy for three locations. For the reactor, the power is set to 50 MWt and the fuel composition is that for a pressurized water reactor, using the Huber model for the emitted reactor spectrum. Each of the positron-detection-efficiency curves shown (in the top plot) is generated assuming a minimum number of PMT hits. The PMT-hit threshold can be optimized for different detector sizes. The details of this optimization are presented in Sec. II. The geoneutrinos (Geo) are invisible in water Cherenkov detectors (for geoneutrinos, a location at Fréjus is shown as an example).

To obtain IBD event rates in a realistic detector, we implement an algorithm approximated by the formula

$$R_d = \left(\int R_e \sigma_{\text{IBD}} P_{\text{surv}} \frac{1}{4\pi L^2} \epsilon_+ \, dE_+ \right) \epsilon_n N_t f_{2\,\text{m}} f_{100\,\mu\text{s}}, \quad (3)$$

where R_d is the IBD detection rate, R_e is the emitted antineutrino spectrum (taking into account the reactor power and fuel composition), σ_{IBD} is the IBD cross section (a function of energy), P_{surv} is the antineutrino survival probability (a function of energy and distance), L is the distance between the reactor and the detector, ϵ_+ is the positron detection efficiency (a function of energy), E_+

TABLE III. Fuel composition (fission fractions) and energy release per fission used in this study.

	^{235}U	^{238}U	^{239}Pu	^{241}Pu
Fission fraction	0.56	0.08	0.30	0.06
Energy/fission (MeV)	201.9	205.0	210.9	213.4

is the positron energy, ϵ_n is the neutron detection efficiency, N_t is the number of targets (hydrogen nuclei) in the fiducial volume, $f_{2\,\text{m}}$ is the 2-m spatial-proximity coefficient (in the range of 91%–98%), and $f_{100\,\mu\text{s}}$ is the 100-μs temporal-proximity coefficient (set at 98%). The fuel composition is kept constant in this study, and is listed in Table III.

II. DETECTOR DESCRIPTION

In the following, we investigate the sensitivity of large water Cherenkov detectors doped with gadolinium. We are interested in estimating the detector size required to successfully detect within one year a test reactor at various distances. In all cases, the assumed detector has the shape of a right cylinder (like Super-K), with a photocoverage fixed at 40%. The veto thickness (to suppress cosmogenic spallation neutrons from the surrounding rock) is fixed at 2 m. The inner detector is also a right cylinder. The PMTs are modeled on 10-inch Hamamatsu 7081 PMTs equipped with low-activity glass. An average dark rate of 3 kHz per PMT is assumed, based on internal measurements of a selection of about a hundred PMTs. All inward-facing PMTs are placed perpendicular to the wall. The fiducial-volume boundary is placed at 2 m from the PMT wall to reduce PMT-based radiation background.

Event-position reconstruction is done using a software package adapted from Super-K called BONSAI [33]. For a given event energy, the detector response depends somewhat on the event position. However, for small detectors, the detector response over the fiducial volume is approximately constant. For large detectors, light attenuation can become significant, and so the response for events in the center of the detector is generally slightly smaller than the response near the edge of the fiducial volume.

TABLE IV. Simulated detector geometries. The fiducial volume is defined as 4 m from the outer tank or 2 m from the PMTs.

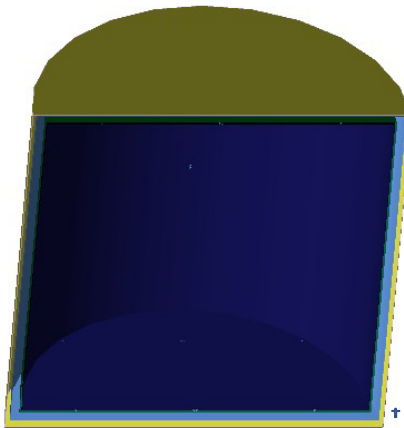| d (m) × h (m)	m (kt)	m_f (kt)	No. of 10-inch PMTs
15 × 15	2.7	0.3	4 512
20 × 20	6.2	1.4	9 516
30 × 30	21.2	8.4	25 182
40 × 40	50.3	25.7	48 258
50 × 50	98.2	58.2	78 856

FIG. 4. GEANT4 (RAT-PAC) visualization of one of the detector geometries. The distance (outer veto region) between the inner tank and the outer tank is kept at 2 m in all simulations. In this particular view, a cutaway view of the 50×50 geometry is presented, with only a few 10-inch PMTs (small dots in the image) to demonstrate the scale. A figure of a person is shown approximately to scale.

Nevertheless, in the present work we use the approximation that the number of photons detected within a Cherenkov wavefront is proportional to the energy of the (minimum-ionizing) particle. To count Cherenkov photons, the time residuals of the position reconstructions are used: n_9 is the number of PMTs with time residuals between -3 and $+6$ ns (the values are chosen based on the PMT timing uncertainty and the expected light scattering). In the following, n_9 serves as a rough energy estimator. The parameter n_9 is modeled after a similar parameter used at Super-K [34,35], using a larger time range (18 ns). A smaller time window is considered appropriate for this study due to the improved time resolution of the Hamamatsu 10-inch PMTs. A set of detector geometries with fiducial volumes between 0.3 and 58 kt are studied here, and are listed in Table IV.

A GEANT4-based simulation package called RAT-PAC [36] is used throughout this study. While based on GEANT4 [37], it includes useful features specifically designed for reactor-antineutrino detector simulations. It was recently further adapted by the WATCHMAN collaboration [16]. A visualization of a 50×50 geometry is shown in Fig. 4.

Physics events in the few MeV region only produce a few dozen PEs. Most PMTs register only one PE. Figure 5 shows the relation between the n_9 parameter and the true positron energy, as simulated in RAT-PAC, along with a plot of energy resolution versus the energy.

IBD event candidates are selected on the basis of the following characteristics: (1) the prompt signal, (2) the delayed signal, (3) the position in the detector, and (4) the time and distance between correlated pairs. A summary of the analysis cuts used is presented in Table V. In order to simplify the analysis and aid in scaling the sensitivity between each of the simulated detector sizes, it is decided to fix some of the analysis cuts *a priori*. For example, the fiducial volume is defined to extend to 4 m from the tank wall for all detector sizes. The maximum distance and time between correlated event pairs are defined to be 2 m and 100 μs, respectively. These initial guesses are informed by an initial round of simulations, which indicate limited sensitivity to detector size. The remaining analysis cuts, the n_9 prompt and delayed cuts, are somewhat dependent on the detector size. However, in the interests of simplicity, since the n_9 prompt cut is found to be the most sensitive one to the detector performance, we opt to optimize only the n_9 prompt, while setting the n_9 delayed cut to a reasonable constant value (where possible). An optimization of the n_9 prompt analysis cut is performed for each detector size (using the detector dwell time as the metric), maintaining all the other analysis cuts constant, as shown in Fig. 6. The primary detector background that impacts the n_9-prompt-cut optimization originates from radioactive decays in the PMT glass and the detection medium. The central regions of the detector medium can be expected to be relatively radiopure [38]. Our simulations assume levels of trace radioactive nuclei in the water consistent with Super-K. This results in a low (but still significant) background event rate. The primary source of background events is due to the ^{238}U and ^{232}Th decay chains. The most problematic isotopes are ^{214}Bi, ^{212}Bi, and ^{208}Tl.

A. Detection efficiency

As mentioned previously, five distinct detector sizes are simulated. The first step in this process is to generate a set of efficiency curves for positrons and neutrons. For each configuration in Table IV, positrons are simulated with a flat [0, 10]-MeV spectrum, distributed uniformly in the detector fiducial volume. A set of efficiency curves is then generated and parametrized using a combination of two

TABLE V. Prompt n_9 cuts obtained using optimization for five different detector sizes, as well as 2-m bubble fractions used in estimation of IBD-like accidental backgrounds. The IBD spatial- and temporal-proximity coefficients are also listed, as used in the IBD signal and background calculations. For any detector size less than 50×50, it is possible to estimate values by interpolation between these detector sizes.

Geometry	$n_{9\ pr}$	$n_{9\ del}$	2-m fraction	$f_{2\ m}$	$f_{100\ \mu s}$
15×15	17	25	0.05256	99%	98%
20×20	17	25	0.02469	99%	98%
30×30	18	25	0.00401	97%	98%
40×40	20	25	0.00130	94%	98%
50×50	26	26	0.00058	91%	98%

Geometry: 20×20

Fit: 12.87 hits/MeV
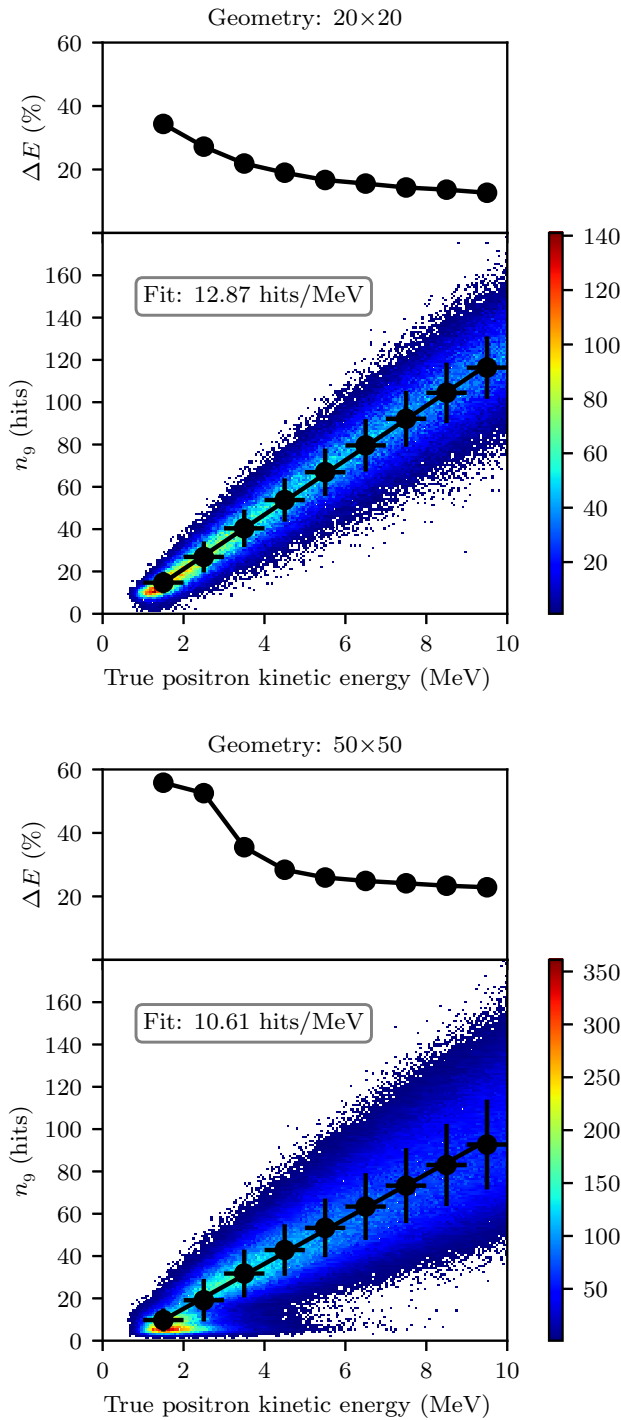

Geometry: 50×50

Fit: 10.61 hits/MeV

FIG. 5. Reconstructed number of PMT hits within a 9-ns window (n_9 parameter) versus positron kinetic energy (Monte Carlo true) for a flat [0, 10]-MeV positron spectrum in the fiducial volume. A detector trigger threshold of 10 PMT hits is applied. Top panel: 20×20 geometry; bottom panel: 50×50. The comparison shows that a degradation in the energy resolution ΔE accompanies increased detector sizes. The large number of events in the bottom left corner of the plot for the 50×50 geometry indicates misreconstruction of low-energy events.
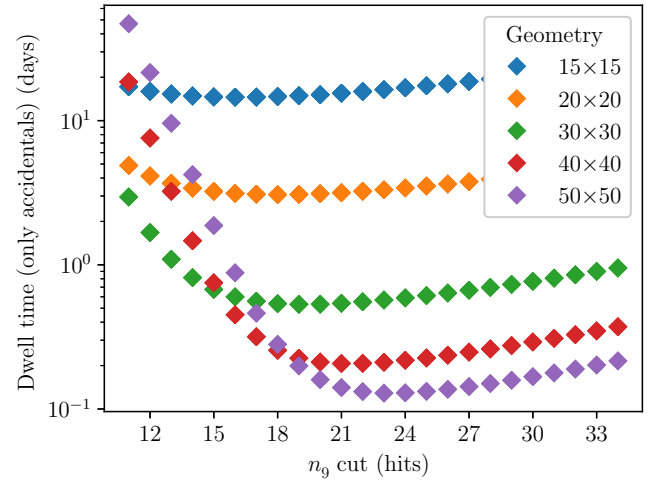

FIG. 6. The dwell time metric based on the Currie equation (described in Sec. III), calculated by varying only the n9 cut on the prompt (applied to both signal and background) while fixing all the remaining cuts. For the 50×50 geometry, an optimal n_9 cut of 26 is chosen to eliminate the effect of the PMT dark rate.

Fermi functions:

$$\epsilon = \frac{1}{2}\left[\frac{1 + \mathrm{sign}(E - b)}{1 + \exp[-a_0(E - b)]} + \frac{1 + \mathrm{sign}(-E + b)}{1 + \exp[-a_1(E - b)]}\right], \quad (4)$$

where E is the positron kinetic energy and "sign" is a sign function, such that $\mathrm{sign}(x) = \pm 1$ if $x \gtrless 0$. For each n_9-parameter cut and each *simulated* geometry, we obtain efficiency curves and a set of stored fit parameters a_0, a_1, and b in a lookup table. The coefficient b is the energy at 50% efficiency. A set of positron efficiency curves are shown in Fig. 7 for an n_9 cut of 26 PEs. The positron efficiency curves shown in Fig. 3 are generated using the optimized n_9 thresholds presented in Table V. For intermediate detector sizes, one can estimate values using interpolations.

B. Detected signal and background events

One source of IBD-like backgrounds is accidental coincidences of gamma rays and neutrons generated by radioactive decays occurring in the detector materials. These consist of two categories:

(a) *volume:* these originate due to radioactive contaminants in the water (Rn, U, Th, and K);

(b) *surface:* these originate from the PMTs due to radioactivity of the glass.

A full chain of simulations is performed to find the rates of these backgrounds for a representative set of detector sizes up to 50×50. Secular equilibrium is assumed between
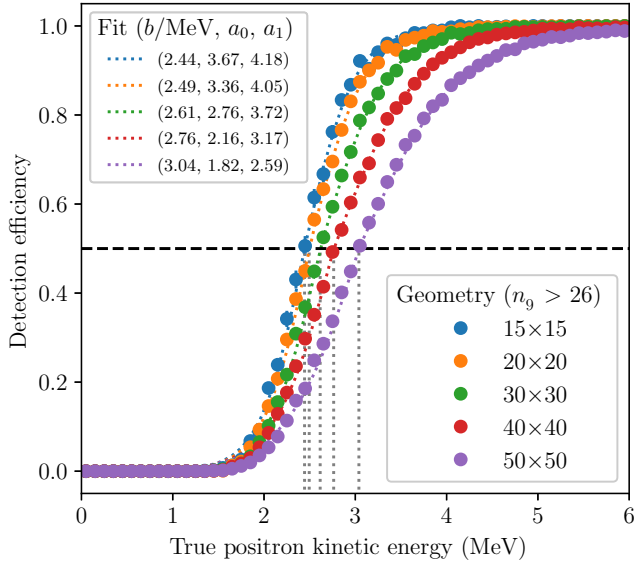
FIG. 7. Positron detection efficiency as a function of Monte Carlo positron kinetic energy. Efficiency curves for $n9 > 26$ are shown as an example here. The vertical dashed lines correspond to the energies at the 50% efficiency level—the parameter b in the fit.

the concentrations of U and Th and the resultant daughter decays. In RAT-PAC, the full U and Th decay chains are included. The assumed radiopurities for water and the PMT glass are listed in Table VI. The PMT values are obtained from measurements of Hamamatsu R7081 PMTs. The water values are chosen to be consistent with previous water-based experiments such as SNO [39] and Super-K [15,35].

The detectors considered here are assumed to be placed at a depth roughly consistent with the proposed depth of the WATCHMAN experiment in the Boulby mine (approximately 2.8 km water equivalent). At this depth, and assuming that the detector fiducial volumes are protected by 4 m of veto and a PMT buffer as described above, cosmogenic fast-neutron backgrounds are expected to be subdominant. Muons, when interacting with the detector medium, can create long-lived isotopes (e.g., ^{8}He and ^{9}Li) that can potentially look like IBD events. At the Boulby depth, these can be effectively vetoed with minimal loss in live time.

The rate of fast neutrons originating from muons interacting with the surrounding rock material is estimated using the Mei-Hime model [40]. A FLUKA simulation is performed to determine the rate and positions of neutron captures inside the 20×20 detector, and then the results are scaled with the fiducial area. We estimate the rate of dineutron events (which could mimic an IBD) as follows:

$$M_i = \sum_j A_{ij} P_j, \qquad (5)$$

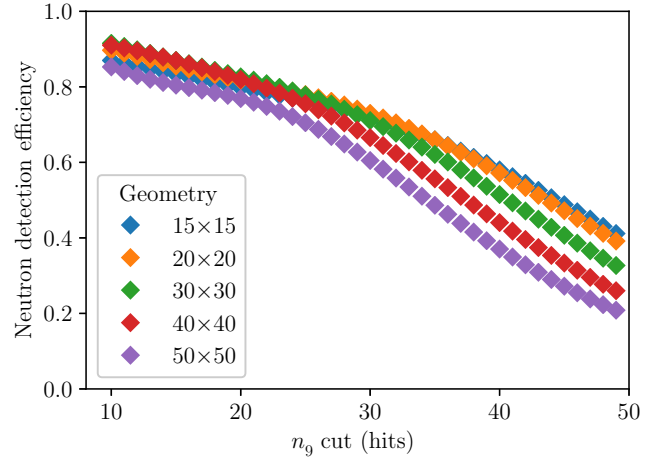$$A_{ij} = \epsilon^i (1 - \epsilon)^{j-i} \binom{j}{i}, \qquad (6)$$

FIG. 8. Neutron detection efficiency as a function of n_9 cut and detector size (a fiducial cut is applied).

where M_i is the measured multiplicity (for detecting two neutrons, $i = 2$), P_j is the produced multiplicity (for producing j neutrons), $\binom{j}{i} = j\,!/[i!(j - i)!]$ is a binomial coefficient, and ϵ is the detection efficiency, taken from Fig. 8 (a mean value is chosen corresponding to optimal n_9 values for prompt and delayed signals).

The rates of exotic backgrounds such as those from diffuse relic-supernova antineutrinos and atmospheric neutrino-induced neutral-current interactions are unknown, although they are constrained to be small [24, 41,42]. As such, these rates are estimated as follows: 4 (events/10 kt)/yr (atmospheric neutrinos scatter off oxygen nuclei) and 2 (events/10 kt)/yr (diffuse supernova-relic antineutrinos). The uncertainties in these two types of backgrounds are expected to be significantly smaller in the near future, as Super-K-Gd will likely measure them within the next few years.

In principle, the requirement that IBD event pairs be reconstructed within 2 m places a significant limitation on the number of uncorrelated detector background events that result in an IBD-like event (see Fig. 9). The fraction of events that pass this criterion is calculated from a simulation for a selection of representative detector sizes and plotted as a function of the n_9 cut. The results are presented in Fig. 10. The expectation is that, for each detector size, this fraction should be independent of the n_9 cut. However, for the larger detector sizes of 40×40 and 50×50,

TABLE VI. Radiopurity levels used in the calculations.

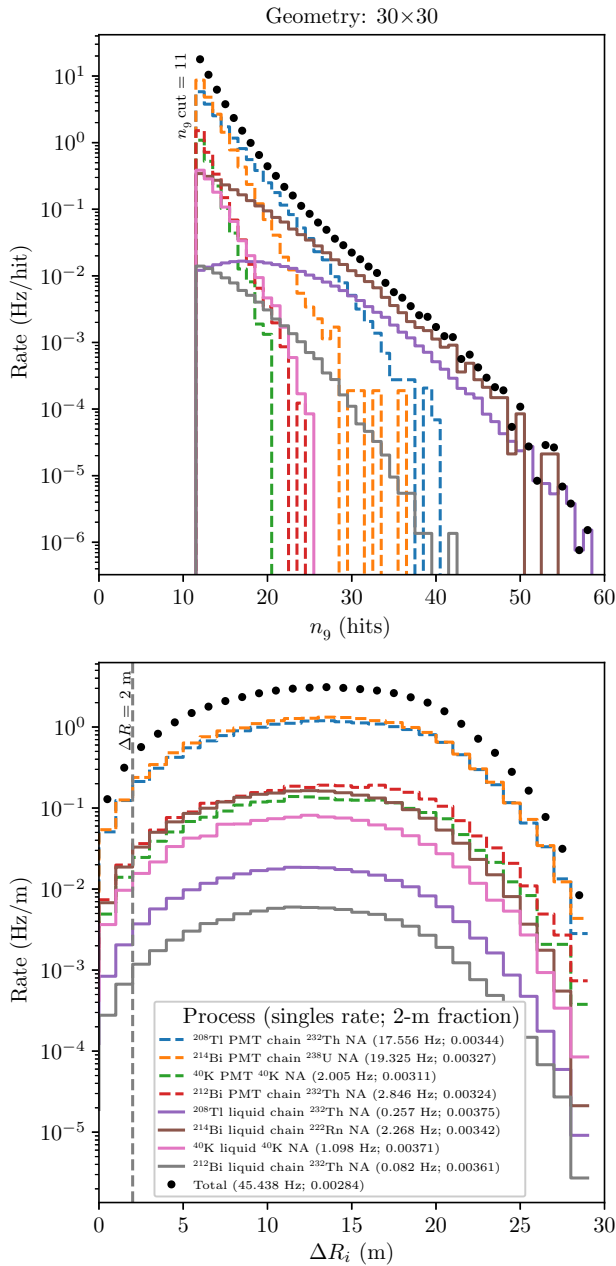| Medium	^{238}U	^{232}Th	^{40}K	^{222}Rn
Water (Bq/kg)	1.0×10^{-6}	1.0×10^{-7}	4.0×10^{-6}	1.0×10^{-6}
PMT (Bq/PMT)	2.45×10^3	2.49×10^3	5.85×10^{-1}	

FIG. 9. Uncorrelated detector background (singles rate) inside the fiducial volume as a function of the n_9 parameter for 30×30 geometry. The primary contributing processes in the PMTs and water are shown. The bottom panel shows, also for a 30×30 detector, an example distribution (for an n_9 cut of 11) of the distance between any two consecutive uncorrelated detector background events that reconstruct inside the fiducial volume. A line is drawn at the 2-m distance cut. The legend is shared between the two plots (NA stands for natural abundance).

it appears that these two parameters are not independent. The reason appears to be that for large detectors, there are a significant number of PMT hits caused by the PMT dark rate (see Figs. 10 and 11). These dark-rate-induced

PMT events severely impact event reconstruction, causing many low-n_9 events to be pushed towards the center of the detector. While the dark rate appears to be the cause, the effect can be removed by applying a higher-n_9 analysis cut (see Table V). For the 50×50 geometry, an optimal n_9 cut of 26 is chosen to eliminate the effect of the PMT dark rate. To determine the minimum-n_9 analysis cut, we calculate the ratio of the 2-m volume to the fiducial volume. When the n_9 cut applied in the simulation results in an equivalent 2-m fraction (within uncertainty), it is assumed to be sufficient to correct for the effect.

For extremely large detector geometries, such as those greater than 50×50, the PMT dark rate of 3 kHz begins to impact the vertex reconstruction algorithm. The effect of this can be seen in Figs. 5 and 10. For these detectors, either new ways must be found to reduce the PMT dark rate or larger-diameter PMTs must be used. For large detectors, the large number of PMTs combined with a high dark rate causes events to preferentially reconstruct near the center of the detector, as demonstrated in Fig. 11.

III. RESULTS AND DISCUSSION

We use the Currie equation [43,44] to evaluate the number of signal events required to register a significant detection. The Currie equation can be generalized to the total uncertainty in the background, including the statistical and systematic uncertainty, as follows:

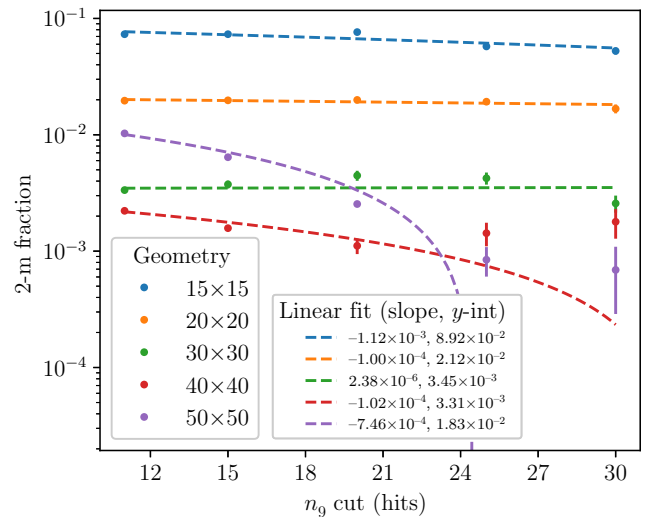$$N_D = 4.653\sigma_B + 2.706. \qquad (7)$$

FIG. 10. Fraction of detector-induced accidental background events within a 2-m volume as a function of n_9 cut for different geometries. Error bars are calculated as follows: $\delta f = 1/\sqrt{\sum N_i R_i / R_{\text{tot}}}$, where N_i is the number of events within a 2-m distance of each other, R_i is the rate of the ith process, and R_{tot} is the total rate (after applying fiducial-volume and n_9 cuts).
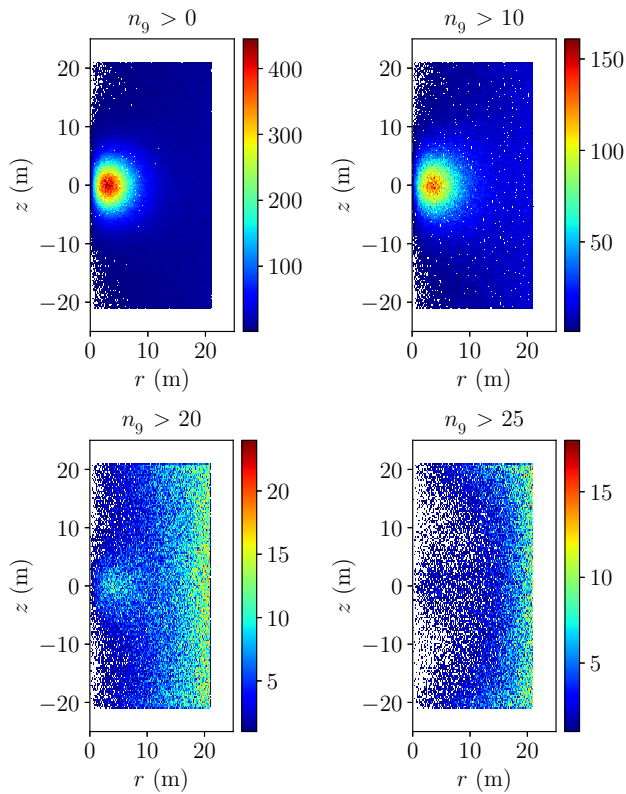
FIG. 11. Spatial distributions of events originating in water due to ^{208}Tl decays in the 50×50 detector (reconstructed position z vs $r = \sqrt{x^2 + y^2}$). The events that reconstruct in the middle of the detector (top panel) are due to the high PMT dark rate affecting the reconstruction algorithm. If the value for the n_9 cut is increased, the reconstruction works better.

The total uncertainty σ_B has statistical and systematic uncertainties added in quadrature:

$$\sigma_B^2 = \sigma_{\text{stat}}^2 + \sigma_{\text{sys}}^2 = N_B + (N_B\delta)^2, \qquad (8)$$

and so

$$N_D = 4.653\sqrt{N_B}\sqrt{1 + N_B\delta^2} + 2.706, \qquad (9)$$

where N_D is the minimum number of counts from the source (antineutrinos from a 50-MWt reactor) required to ensure reliable detection in the presence of background, and N_B is the total background, including world reactors, uncorrelated detector backgrounds, cosmogenic fast neutrons, atmospheric neutrino interactions with oxygen, diffuse supernova antineutrinos, and geological antineutrinos. We assume that the systematic uncertainty δ is symmetric, ensuring that the underlying assumptions used to derive the Currie equation remain valid (i.e., systematic and statistical uncertainties can be added in quadrature, and the total systematic uncertainty remains Gaussian). For low-count circumstances such as for short dwell times or
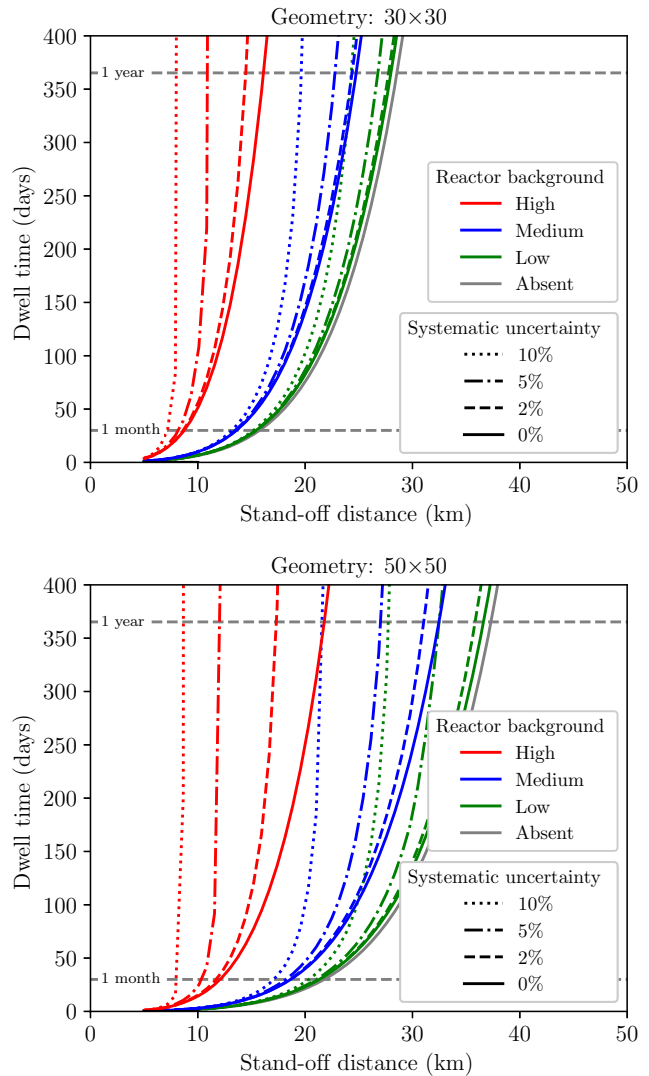

FIG. 12. Dwell time for two different geometries (30×30 and 50×50) as a function of stand-off distance to a 50-MWt reactor. The color represents the world reactor background. The line style represents four different levels of systematic uncertainty (0%, 2%, 5%, and 10%), based on Eq. (9). For clarity, the systematic effects are not shown for the "absent" world-reactor-background curve. The Gaussian assumption remains valid for dwell times greater than approximately one month. For smaller dwell times, a Poisson treatment is more accurate.

long baselines, the systematic uncertainty δ can have an important impact on N_D. The dwell time as a function of distance and the effect of adding nonzero systematic uncertainties ($\delta = 2\%$, 5%, and 10%) are shown in Fig. 12.

The flux and spectrum of reactor antineutrinos for any reactor-detector distance are calculated by applying up-to-date neutrino-oscillation parameters as shown in Fig. 1. Since the worldwide reactor flux background can vary considerably depending on where in the world the detector is placed, three locations are chosen as broadly representative of three reactor-background cases: high, medium, and
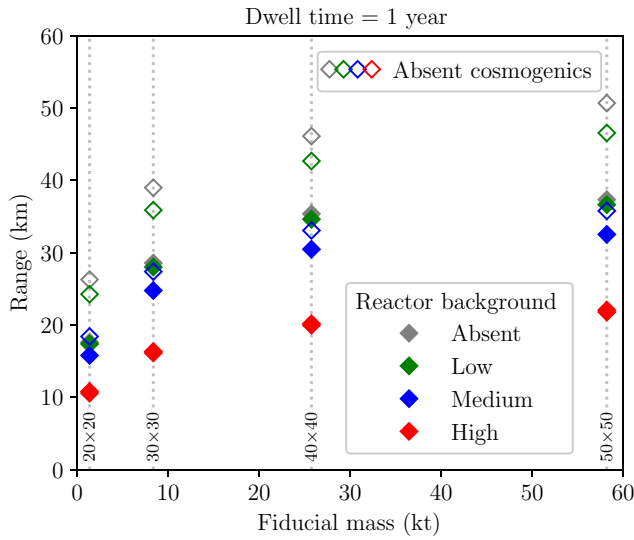
FIG. 13.   Range as a function of stand-off distance for a 1-year dwell time with three world reactor backgrounds. The empty diamonds indicate scenarios with zero cosmogenic fast-neutron background.

low. The three locations chosen are the Andes, Baksan, and Fréjus underground laboratories. The web tool geoneutrinos.org is used to calculate the world reactor antineutrino fluxes in those locations [45]. Unlike detector backgrounds, antineutrino backgrounds cannot be removed by applying clever analysis cuts, and so the world's reactors comprise an important and irreducible background in these calculations.

Other important performance parameters needed for this analysis are the detector background rates as a function of n_9 (energy) (Fig. 9), and the fraction of uncorrelated detector backgrounds that reconstruct inside the fiducial volume within the 2-m proximity requirement for IBD events. Figure 9 also shows the distribution of uncorrelated detector backgrounds as a function of the distance from the previous event for a variety of different detector backgrounds.

For locations with a high world reactor background (e.g., the Fréjus site at the border between France and Italy), the task of detecting a small 50-MWt reactor at a large distance depends primarily on the world reactor background at that location. This is the primary reason why the estimated range levels off as a function of detector size in Fig. 13.

All other backgrounds, such as those associated with detector radiopurity and cosmogenic interactions, are found to be subdominant for the Fréjus location. Although geological antineutrinos are included in the calculations, they are easily rejected, as their energies are either below the detection threshold or not far enough above it to produce an energetic enough event for detection. Table VII shows the numbers of signal and background events for each detector location. The signal values presented in Table VII are calculated using Eq. (3), where the positron, neutron, spatial, and temporal efficiencies are based on Figs. 3 and 8 and Table V.

One significant outcome of this work is that it is clear that water Cherenkov detectors, despite the clarity of the detection medium, seem to approach a sensitivity limit at the 50×50 scale (as shown in Fig. 13). Detectors of this scale appear to level off in sensitivity at approximately 50 km due to a combination of neutrino oscillations, which become significant at that distance, the PMT dark rate, and detector self-absorption, which appears to impact performance at the 50×50 scale. The problem of the negative effect of the PMT dark rate on event reconstruction severely impacts sensitivity in this work. However, improvements in event reconstruction algorithms might be able to overcome this difficulty [46], but such improvements, if achievable, are considered to be outside the scope of this work.

TABLE VII.   Number of counts per year for signal and various backgrounds in the simulated detector geometries. The annual signal rates are reported for 10, 20, and 50-km baselines.

Detector		Signal (50 MWt)			Background						
$D \times H$	m_{fid}/kt	10-km	20-km	50-km	World reactor			Accidental	Cosmogenic	Exotic	Geo
					Low	Medium	High				
20×20	1.3	89	20	2	2	19	248	2	24	1	< 1
30×30	8.4	498	113	9	11	105	1388	7	81	5	2
40×40	25.7	1232	280	23	26	258	3397	17	165	15	3
50×50	58.2	1614	372	34	33	324	4017	2	247	35	3

Mark Duvall for help with visualization of large geometries in RAT-PAC. All computations were performed on the Livermore-Computing Lassen cluster running the Red Hat Linux operating system. Analysis routines were written using ROOT 6 [47] and Python 3, primarily with the NumPy [48], SciPy [49], Pandas [50], and Matplotlib [51] packages.

[1] A. A. Borovoi and L. A. Mikaelyan, Possibilities of the practical use of neutrinos, Sov. At. Energy **44,** 589 (1978).

[2] E. Fermi, An attempt of a theory of beta radiation, Z. Phys. **88,** 161 (1934).

[3] S. E. Bays, G. A. Reyes, M. J. Schanfein, R. H. Stewart, and N. P. Martin, Significant quantity production rates in small modular reactors, Proc. INMM ESARDA Joint Virtual Annu. Meeting (2021).

[4] IAEA, in *Advances in Small Modular Reactor Technology Developments* (IAEA, Austria, 2020).

[5] C. L. Cowan, F. Reines, F. B. Harrison, H. W. Kruse, and A. D. McGuire, Detection of the free neutrino: A confirmation, Science **124,** 103 (1956).

[6] F. Boehm, J. Busenitz, B. Cook, G. Gratta, H. Henrikson, J. Kornis, D. Lawrence, K. B. Lee, K. McKinny, and L. Miller, *et al.* (Palo Verde), Search for Neutrino Oscillations at the Palo Verde Nuclear Reactors, Phys. Rev. Lett. **84,** 3764 (2000).

[7] M. Apollonio, A. Baldini, C. Bemporad, E. Caffau, F. Cei, Y. Déclais, H. de Kerret, B. Dieterle, A. Etenko, and L. Foresti, *et al.* (CHOOZ), Search for neutrino oscillations on a long baseline at the CHOOZ nuclear power station, Eur. Phys. J. **C27,** 331 (2003).

[8] Y. Abe, C. Aberle, T. Akiri, J. C. dos Anjos, F. Ardellier, A. F. Barbosa, A. Baxter, M. Bergevin, A. Bernstein, and T. J. C. Bezerra, *et al.* (Double Chooz), Indication of Reactor $\bar{\nu}_e$ Disappearance in the Double Chooz Experiment, Phys. Rev. Lett. **108,** 131801 (2012).

[9] F. P. An, J. Z. Bai, A. B. Balantekin, H. R. Band, D. Beavis, W. Beriguete, M. Bishai, S. Blyth, K. Boddy, and R. L. Brown, *et al.* (Daya Bay), Observation of Electron-Antineutrino Disappearance at Daya Bay, Phys. Rev. Lett. **108,** 171803 (2012).

[10] J. K. Ahn, S. Chebotaryov, J. H. Choi, S. Choi, W. Choi, Y. Choi, H. I. Jang, J. S. Jang, E. J. Jeon, and I. S. Jeong, *et al.* (RENO), Observation of Reactor Electron Antineutrino Disappearance in the RENO Experiment, Phys. Rev. Lett. **108,** 191802 (2012).

[11] T. Araki, K. Eguchi, S. Enomoto, K. Furuno, K. Ichimura, H. Ikeda, K. Inoue, K. Ishihara, T. Iwamoto, and T. Kawashima, *et al.* (KamLAND), Measurement of Neutrino Oscillation with KamLAND: Evidence of Spectral Distortion, Phys. Rev. Lett. **94,** 081801 (2005).

[12] F. An, G. An, Q. An, V. Antonelli, E. Baussan, J. Beacom, L. Bezrukov, S. Blyth, R. Brugnera, and M. Buizza Avanzini, *et al.* (JUNO), Neutrino physics with JUNO, J. Phys. G **43,** 030401 (2016).

[13] M. Baldoncini, V. Strati, S. A. Wipperfurth, G. Fiorentini, F. Mantovani, W. F. McDonough, and B. Ricci, Geoneutrinos and reactor antineutrinos at SNO+, J. Phys. Conf. Ser. **718,** 062003 (2016).

[14] K. C. Abe, C. Bronner, Y. Hayato, K. Hiraide, M. Ikeda, S. Imaizumi, J. Kameda, Y. Kanemura, Y. Kataoka, and S. Miki, *et al.* (Super-Kamiokande), First gadolinium loading to Super-Kamiokande, Nucl. Instrum. Meth. A **1027,** 166248 (2022).

[15] L. Marti, M. Ikeda, Y. Kato, Y. Kishimoto, M. Nakahata, Y. Nakajima, Y. Nakano, S. Nakayama, Y. Okajima, and A. Orii, *et al.*, Evaluation of gadolinium's action on water Cherenkov detector systems with EGADS, Nucl. Instrum. Meth. A **959,** 163549 (2020).

[16] M. Askins, M. Bergevin, A. Bernstein, S. Dazeley, S. T. Dye, T. Handler, A. Hatzikoutelis, D. Hellfeld, P. Jaffke, and Y. Kamyshkov, *et al.* (WATCHMAN), The Physics and Nuclear Nonproliferation Goals of WATCHMAN: A WAter CHerenkov Monitor for ANtineutrinos, (2015), ArXiv:1502.01132.

[17] P. A. Cherenkov, Visible luminescence of pure liquids under the influence of gamma-radiation, Dokl. Akad. Nauk SSSR **2,** 451 (1934). [Usp. Fiz. Nauk 93, 385 (1967)]

[18] I. M. Frank and I. E. Tamm, Coherent visible radiation of fast electrons passing through matter, Dokl. Akad. Nauk SSSR **14,** 109 (1937). [Usp. Fiz. Nauk 93, 388 (1967)]

[19] K. Hagiwara, T. Yano, T. Tanaka, M. S. Reen, P. K. Das, S. Lorenz, I. Ou, T. Sudo, Y. Yamada, and T. Mori, *et al.*, Gamma ray spectrum from thermal neutron capture on gadolinium-157, PTEP **2019,** 023D01 (2019).

[20] T. Tanaka, K. Hagiwara, E. Gazzola, A. Ali, I. Ou, T. Sudo, P. K. Das, M. S. Reen, R. Dhir, and Y. Koshio, *et al.*, Gamma ray spectra from thermal neutron capture on gadolinium-155 and natural gadolinium, PTEP **2020,** 043D02 (2020).

[21] R. M. Pope and E. S. Fry, Absorption spectrum (380–700 nm) of pure water. II. Integrating cavity measurements, Appl. Opt. **36,** 8710 (1997).

[22] K. Abe, Y. Hayato, T. Iida, K. Iyogi, J. Kameda, Y. Kishimoto, Y. Koshio, L. Marti, M. Miura, and S. Moriyama, *et al.*, Calibration of the Super-Kamiokande detector, Nucl. Instrum. Meth. A **737,** 253 (2014).

[23] A. Bernstein, T. West, and V. Gupta, An assessment of antineutrino detection as a tool for monitoring nuclear explosions, Sci. Global Security **9,** 235 (2001).

[24] J. F. Beacom and M. R. Vagins, Anti-neutrino Spectroscopy with Large Water Cherenkov Detectors, Phys. Rev. Lett. **93,** 171101 (2004).

[25] H. Watanabe, H. Zhang, K. Abe, Y. Hayato, T. Iida, M. Ikeda, J. Kameda, K. Kobayashi, Y. Koshio, and M. Miura, *et al.*, First study of neutron tagging with a water Cherenkov detector, Astropart. Phys. **31,** 320 (2009).

[26] S. Dazeley, A. Asghari, A. Bernstein, N. S. Bowden, and V. Mozin, A water-based neutron detector as a well multiplicity counter, Nucl. Instrum. Meth. A **771,** 32 (2015).

[27] H. P. Lima Jr., J. A. M. Alfonzo, J. C. Anjos, G. Cernicchiaro, P. Chimenti, I. A. Costa, M. P. Dias, P. C. M. A. Farias, A. Fernandes Jr., and G. P. Guedes, *et al.*, Neutrinos Angra experiment: commissioning and first operational measurements, J. Instrum. **14,** 06010 (2019).

[28] S. Dazeley, M. Askins, M. Bergevin, A. Bernstein, N. S. Bowden, T. M. Shokair, P. Jaffke, S. D. Rountree, and

M. Sweany, A search for cosmogenic production of beta-neutron emitting radionuclides in water, Nucl. Instrum. Meth. A **821,** 151 (2016).

[29] A. R. Back, J. F. Beacom, M. Bergevin, E. Catano-Mur, S. Dazeley, E. Drakopoulou, F. Di Lodovico, A. Elagin, J. Eisch, and V. Fischer, *et al.* (ANNIE), Accelerator Neutrino Neutron Interaction Experiment (ANNIE), (2017), ArXiv:1707.08222.

[30] A. Strumia and F. Vissani, Precise quasielastic neutrino-nucleon cross-section, Phys. Lett. **B564,** 42 (2003).

[31] P. Huber, On the determination of anti-neutrino spectra from nuclear reactors, Phys. Rev. C **84,** 024617 (2011).

[32] A. Bernstein, N. Bowden, B. L. Goldblum, P. Huber, I. Jovanovic, and J. Mattingly, Colloquium: Neutrino detectors as tools for nuclear security, Rev. Mod. Phys. **92,** 011003 (2020).

[33] M. Smy, (Super–Kamiokande), Low energy event reconstruction and selection in Super-Kamiokande-III, Proc. 30th Int. Cosmic Ray Conf., 1279–1282 (2007).

[34] T. Tomura, Y. Hayato, M. Ikeno, M. Nakahata, S. Nakayama, Y. Obayashi, K. Okumura, M. Shiozawa, S. Y. Suzuki, and T. Uchida, *et al.*, Development of new data acquisition system at Super-Kamiokande for nearby supernova bursts, IEEE Trans. Nucl. Sci. **60,** 3694 (2013).

[35] K. Abe, Y. Haga, Y. Hayato, M. Ikeda, K. Iyogi, J. Kameda, Y. Kishimoto, L. Marti, M. Miura, and S. Moriyama, *et al.* (Super-Kamiokande), Solar neutrino measurements in Super-Kamiokande-IV, Phys. Rev. D **94,** 052010 (2016).

[36] S. Seibert, T. Bolton, D. Gastler, J. Klein, H. Lippincott, A. Mastbaum, J. Nikkel, G. Orebi Gann, M. Akashi-Ronquest, and S. Sekula, *et al.*, RAT-PAC analysis package, online documentation (accessed 2022).

[37] S. Agostinelli, J. Allison, K. Amako, J. Apostolakis, H. Araujo, P. Arce, M. Asai, D. Axen, S. Banerjee, and G. Barrand, *et al.* (GEANT4), GEANT4: A simulation toolkit, Nucl. Instrum. Meth. A **506,** 250 (2003).

[38] Y. Nakano, T. Hokama, M. Matsubara, M. Miwa, M. Nakahata, T. Nakamura, H. Sekiya, Y. Takeuchi, S. Tasaka, and R. A. Wendell, Measurement of the radon concentration in purified water in the Super-Kamiokande IV detector, Nucl. Instrum. Meth. A **977,** 164297 (2020).

[39] N. Jelley, A. B. McDonald, and R. G. Hamish Robertson, The Sudbury Neutrino Observatory, Ann. Rev. Nucl. Part. Sci. **59,** 431 (2009).

[40] D. Mei and A. Hime, Muon-induced background study for underground laboratories, Phys. Rev. D **73,** 053004 (2006).

[41] M. Leyton and S. Dye, Prospects for long-range reactor monitoring with gadolinium-loaded water-Cherenkov detectors, Proc. 13th Int. Workshop Appl. Antineutrino Phys. (2017).

[42] L. Wan, K. Abe, C. Bronner, Y. Hayato, M. Ikeda, K. Iyogi, J. Kameda, Y. Kato, Y. Kishimoto, and L. Marti, *et al.* (Super-Kamiokande Collaboration), Measurement of the neutrino-oxygen neutral-current quasielastic cross section using atmospheric neutrinos at Super-Kamiokande, Phys. Rev. D **99,** 032005 (2019).

[43] L. A. Currie, Limits for qualitative detection and quantitative determination. Application to radiochemistry, Anal. Chem. **40,** 586 (1968).

[44] G. Knoll, *Radiation Detection and Measurement* (Wiley, 2010), 4th ed.

[45] A. Barna and S. Dye, Global Antineutrino Modeling: A Web Application, (2015), ArXiv:1510.05633.

[46] E. Kneale, *Coincidence-based reconstruction and analysis for remote reactor monitoring with antineutrinos*, Ph.D. thesis, University of Sheffield (2021).

[47] R. Brun and F. Rademakers, ROOT: An object-oriented data analysis framework, Nucl. Instrum. Meth. A **389,** 81 (1997).

[48] C. R. Harris, K. J. Millman, S. J. van der Walt, R. Gommers, P. Virtanen, D. Cournapeau, E. Wieser, J. Taylor, S. Berg, and N. J. Smith, *et al.*, Array programming with NumPy, Nature **585,** 357 (2020).

[49] P. Virtanen, R. Gommers, T. E. Oliphant, M. Haberland, T. Reddy, D. Cournapeau, E. Burovski, P. Peterson, W. Weckesser, and J. Bright, *et al.*, SciPy 1.0–Fundamental algorithms for scientific computing in Python, Nat. Meth. **17,** 261 (2020).

[50] W. McKinney, Data structures for statistical computing in Python, Proc. 9th Python Sci. Conf., 56, (2010).

[51] J. D. Hunter, Matplotlib: A 2D graphics environment, Comput. Sci. Eng. **9,** 90 (2007).